· Article · Advances in Polar Science
doi: 10.12429/j.advps.2024.0002 June 2024 Vol. 35 No. 2: 252-263

Methods for ice velocity mapping in West Antarctica using historical optical satellite images

ZHANG Yujie[1,2], AN Lu[1,2*], TANG Leyue[1,2], LI Hongwei[1,2], HE Meixi[1,2] & LI Rongxing[1,2*]

[1] Center for Spatial Information Science and Sustainable Development Applications, Tongji University, Shanghai 200092, China;
[2] College of Surveying and Geo-Informatics, Tongji University, Shanghai 200092, China

Received 14 January 2024; accepted 23 April 2024; published online 30 June 2024

Abstract The Antarctic Ice Sheet harbors more than 90% of the Earth ice mass, with significant losses experienced through dynamic thinning, particularly in West Antarctica. The crucial aspect of investigating ice mass balance in historical periods preceding 1990 hinges on the utilization of ice velocities derived from optical satellite images. We employed declassified satellite images and Landsat images with normalized cross correlation based image matching, adopting an adaptive combination of skills and methods to overcome challenges encountered during the mapping of historical ice velocity in West Antarctica. A basin-wide synthesis velocity map encompassing the coastal regions of most large-scale glaciers and ice shelves in West Antarctica has already been successfully generated. Our results for historical ice velocities cover over 70% of the grounding line in most of the West Antarctic basins. Through adjustments, we uncovered overestimations in ice velocity measurements over an extended period, transforming our ice velocity map into a spatially deterministic, temporally average version. Among all velocity measurements, Thwaites Glacier exhibited a notable spatial variation in the fastest ice flowline and velocity distribution. Overestimation distributions on Thwaites Glacier displayed a clear consistency with the positions of subsequent front calving events, offering insights into the instabilities of ice shelves.

Keywords **Antarctica**, **ice velocity**, **overestimation correction**, **historical imagery**

Citation: Zhang Y J, An L, Tang L Y, et al. Methods for ice velocity mapping in West Antarctica using historical optical satellite images. Adv Polar Sci, 2024, 35(2): 252-263, doi: 10.12429/j.advps.2024.0002

1 Introduction

The availability of declassified military intelligence photographs dating back to the 1960s, made accessible since 1995, along with Landsat imagery from 1972, played a pivotal role in enabling comprehensive studies of ice motion at glacier-scale, basin-scale and continental scale in Antarctica before 1990. The Antarctic coast product derived from ARGON imagery provided an approximate spatial coverage of declassified intelligence satellite photograph (DISP) ARGON imagery, delineating areas where ice motions could be estimated (Kim, 2004). Wang et al. (2016, 2022) extended the ice velocity records of Larsen Ice Shelf, reaching back to the 1960s–1970s from orthorectified ARGON images and others sources. Li et al. (2017) introduced a new novel parallax decomposition strategy for stereo ARGON photographs and developed a hierarchical matching approach. Further work uncovered overestimation in ice velocities measurements over a long-time span, a critical finding for regions with high dynamism. This overestimation could be quantified and subsequently

* Corresponding authors, ORCID: 0000-0003-3507-5953, E-mail: anlu2021@tongji.edu.cn (AN Lu); ORCID: 0000-0001-9837-5115, E-mail: rli@tongji.edu.cn (LI Rongxing)

corrected within a Lagrangian framework (Li et al., 2022). As Heid and Kääb (2012) suggested a more focus on intelligent post-processing and filter procedures, emphasizing their importance over pure algorithms, we had mapped accurate ice velocities on East Antarctica with optimizing normalized cross correlation based (NCC-based) matching strategies. Experiments conducted on the Fimbul and Jelbart ice shelves have illustrated the efficacy of hierarchical network constraints in enhancing the tracking of ice displacement on historical optical satellite images (Feng et al., 2023). Notably, a comparative analysis on the Byrd Glacier revealed improved spatial coherence among neighboring points with the application of hierarchical constraints in dense matches (Yuan et al., 2023). In the case of the Totten Ice Shelf, acceleration patterns since 1963 near the grounding line exhibited a significant correlation with basal melting, and accidental fast flowing observed on the shelf front due to calving front retreat was accurately detected and corrected (Li et al., 2023).

In this study for glaciers and ice streams velocity mapping in West Antarctica, we met with new challenges as follows. Wide distributed clouds in coastal regions due to lower terrain on West Antarctic Ice Sheet shielded many fields, we had to make full use of every cloud-free and thin-cloud covered image blocks to fill spatial coverage and increase temporal components. Widest, fastest, and most dynamic outlets of Antarctic Ice Sheet were principally distributed in West Antarctica, Ross and Ronne are the largest ice shelves, Getz, Larsen and George VI ice shelves fed by many ice streams extended and occupied a large portion of areas in basin-wide, velocities on Pine Island Glacier (PIG) and Thwaites Glacier were both fast and in acceleration. Thwaites Glacier had extreme wide flowing zone all in high speed, and its ice tongue extended longer into Amundsen Sea, which made it too hard to accurately locate single Landsat images in such cases. Calved ice shelves and accelerated ice flow ever since historical periods lessen prior information that we could get from reference ice velocity measurements in subsequent periods especially in regions with velocities that had significant spatial gradients. Therefore, we targeted to adjust hierarchically constrained NCC-based matching methods to map ice velocities in West Antarctica. Several steps in the process, including control points selection, seed points determination, and match filtering inspections, required interactive manual interventions to enhance accuracy. The initiative aimed to push the boundaries of ice motion estimation back to the earliest possible timeframe, reaching into the 1960s–1980s in West Antarctica.

2 Datasets and methods

2.1 Historical images

In this study, we collected optical satellite images in West Antarctica before 1990. An ARGON mosaic and coastline products of Antarctica was provided by Kee-Tae Kim as an orthorectified version (Kim, 2004), which could directly locate glaciology feature marks in 1963. Landsat images filmed in Antarctica during 1970s and 1980s, archived at the USGS (https://earthexplorer.usgs.gov/), required additional preprocessing, specifical orthorectification.

2.2 Reference datasets

The Landsat Image Mosaic of Antarctica (LIMA) is the geolocation reference for registration of historical Landsat images (Bindschadler et al., 2008). To facilitate terrain correction for these historical Landsat images, the Radarsat Antarctic Mapping Project Digital Elevation Model Version-2 (RAMPv2) was selected (Liu et al., 2015). For additional terrain correction support, the Reference Elevation Model of Antarctica DEM (REMA) was chosen and the version of resolution was 200 m to match the RAMPv2 (Howat et al., 2019). The geographical framework was Antarctic Polar Stereographic (EPSG 3031).

Previous research listed rock outcrops, blue ice areas where ice flow is relatively slow, ice rises, and relatively stable rumples as stable natural ground control points (GCPs) for geolocation registration (Feng et al., 2023). Representative landmarks were referred to methods and datasets as rock outcrops by Gerrish (2020), and blue ice areas by Hui et al. (2014). Existing multi-source velocity maps in Antarctica, such as those proposed by Rignot et al. (2017), provide reference ice velocities in West Antarctica and verify stabilities of regions encompassing these landmarks and temporal consistency.

2.3 Processing methodology

The methodology is structured around three key processing sections: orthorectification for geographical accuracy, velocity measuring by hierarchical matching, and map generation with adjustments. The main processing flow, processing criteria and key techniques employed to obtain a historical synthetic trans-glacial and cross-decade velocity map are illustrated in Figure 1.

2.4 Orthorectification for historical Landsat images

The orthorectification process, including georeferencing, terrain correction, control network estimation and other crucial steps, is detailed in this section. We performed orthorectifications by commercial software PCI Geomatica with bundle adjustment (BA) process based on Toutin's rigorous model (Toutin, 2004). Orthorectified images are rigorously geocoded.

2.4.1 GCP selection

Reference dataset, as mentioned earlier, contribute significantly to feature recognition and distribution analysis, incorporating parameters such as elevation, ice velocity and others. Large ice shelves are located and pinned by ice-enveloped islands. Higher stand ice-enveloped islands

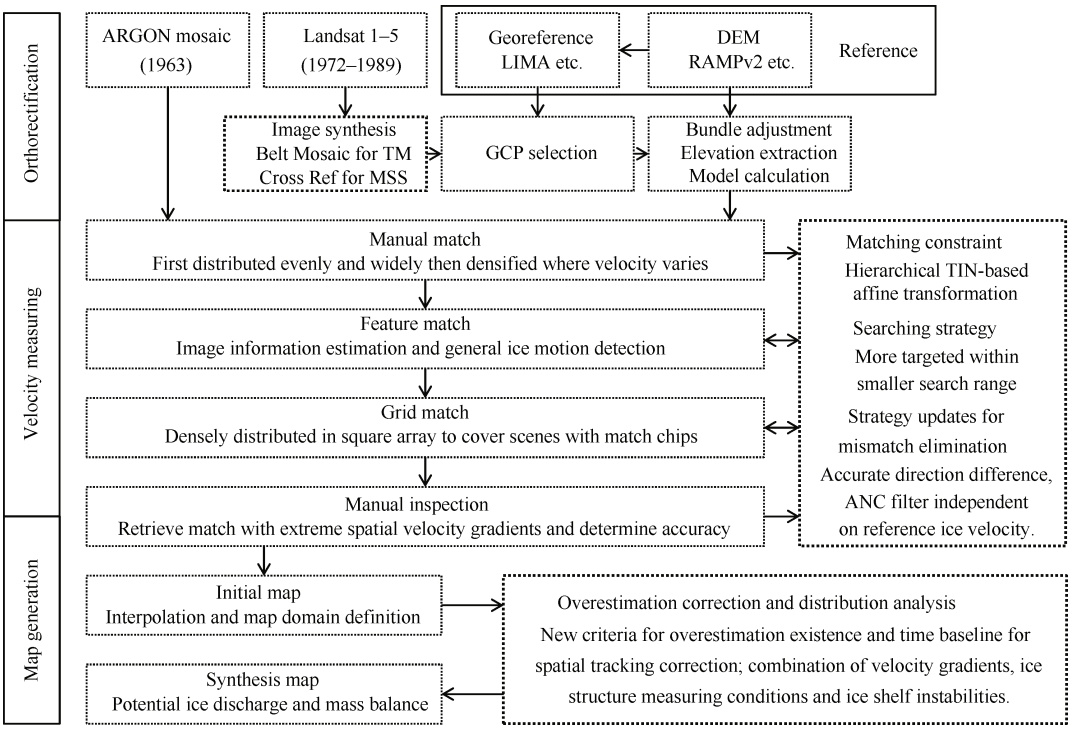

Figure 1 Processing framework for ice velocity mapping in West Antarctica with historical optical satellite images. ANC: adaptive neighboring correlation; TIN: triangle irregular network.

were major source of ice rises. While in scenes with large portions of ocean or flowing ice shelves (Land Ice Tongue, ice shelves on Amundsen Sea, and many ice shelves in Antarctic Peninsula for instance), off-shore islands with stable areas and clear ice-ocean boundaries could be selected as GCPs as well.

Criteria for the order of GCP selection are as follows. The highest priority is rock outcrops and blue ice areas. The second is offshore small islands without accurate elevation data in Radarsat Antarctic Mapping Project (RAMP) and Reference Elevation Model of Antarctica (REMA) and peak-fuzzy ice rises. Finally, simply shaped features where the ice flows at a slower pace. The distribution and geolocation conditions of GCPs are collectively referred to as their network. When the prior options of landmarks are not evenly and broadly distributed within a scene, potential options of GCPs can be considered to optimize the geometric structure of the GCP network, aiming to eliminate new distortions in BA.

2.4.2 Orthorectification for images in West Antarctica

The coastal area of Antarctica exhibited a more favorable scenario for GCP selection, as landmarks were relatively widely distributed, and ice features demonstrated distinct patterns enhanced by ice flow acceleration. That made it possible to measure ice flow velocity accurately in historical periods.

Adjacent along-track Thematic Mapper (TM) images filmed continuously share same contents in overlapping regions, allowing for seamless mosaicking before orthorectification. We limited the mosaic to include at most four adjacent TM images. The residual errors of the BA model might be slightly overestimated in track-along edge in PCI Geomatica. However, through careful validation with the LIMA, we verified that the orthorectified image mosaics were accurate and aligned with high precision indeed.

For adjacent along-track MSS images, it was observed that the overlapping scenes contained the same landscapes or clouds, similar to TM images. Due to inconsistent offsets and opposite side distortions, direct mosaicking or the application of simple geometric transformations before orthorectification was not feasible. With timespan of only a few seconds, any pattern could be selected as GCPs from orthorectified spatial and temporal adjacent images. When the GCP candidates are for adjacent Multispetral Scanner (MSS) scenes, we implemented hierarchical layers of orthorectification to reach higher accuracy. When the geographical information of the orthorectified adjacent images became consistent in overlap areas, the final layer of orthorectification was performed.

For MSS images cross orthorectification, there were not triple overlaps as required in aerial strip block adjustments, therefore the max number of image components is 2. For TM image belt orthorectification, we took curvature of Earth as main influence factor to distinguish belt orthorectification and orthorectified image link. We set i as the number of image components. When we limited the max projection offset as 30 m, and i is solved as 5, therefore we set max value of i as 4 in order to keep tolerance for GCP geolocation errors.

In summary, our orthorectification approach involved the production of a series of orthorectified image belts through mosaic before orthorectification for TM data and an ordered orthorectification strategy for MSS data. These orthorectified image belts effectively covered numerous scenes featuring active ice flows or ocean in the middle. The only limitation emerged in accurately geolocating scenes within the Ross or Ronne ice shelves. When image belts covered the both sides of seams (repeated or missed scene strips) on LIMA, the orthorectified image belts might have better geolocation accuracy than image components of LIMA (Figure 2).

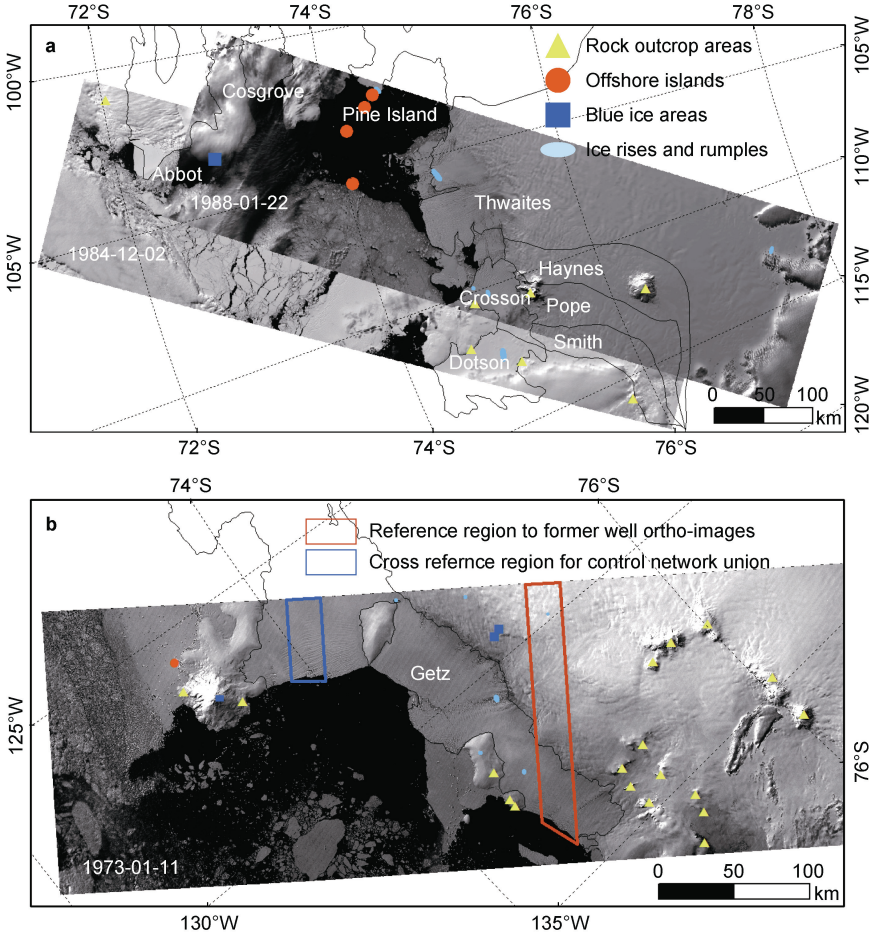

Figure 2 Belt orthorectification for TM images and cross orthorectification for MSS images. **a**, TM image belt in Thwaites Glacier, filmed on 2 December 1984 and 22 January 1988; **b**, MSS image belt in Getz Ice Shelf, filmed on 11 January 1973.

2.5 Velocity measuring

The key step of accurate velocity measurement follows a hierarchical network densification matching strategy that we developed (Feng et al., 2023), employing multi-level recursive matching and tracking executions with detailed constraints.

2.5.1 Match procedures

Our matching methods were designed not specifically to enhance the accuracy for individual match results but rather to significantly increase the overall number of correct matches. There are four main stages of the matching procedure (Figure 1), manual matches were first selected to build the initial Delaunay triangular irregular networks (D-TIN) along with GCPs. Affine transformations, according to TIN, were then applied to indicate the initial locations of ice motion displacement endpoints during timespans of image pairs. Feature matches are extracted by the Shi-Tomasi corner point detection operator and expected to indicate all observable ice flowing channels and improve TIN-based affine constraint. Grid matches were densely generated in square array and expected to fulfill the regions with ice velocity measurements. Manual inspections would be introduced in mismatch eliminations.

In automated matching stages, output results are adjusted by several parameters. Besides constraint, match chip size, search distance threshold, grid interval for program adjustment and image contrast, ambiguity for image pair adjustment were applied. There were almost 8-pixel spatial repeated strip noises in MSS imagery, match chip size was set as 32 pixels as usual and decreased to 16 or 8 when ice flow channels were extremely narrow. Search distance threshold was decreased over match iterations in

one stage, which was first set as maximum displacement in case there were undetected stable regions, and then half-size every time until searching range approached chip size. Grid interval was first set as chip size to fulfill the velocity field and reduced with worse match-retained conditions. Contrast is for adaptive histogram equalization enhancements while it is adjusted by ClipLimit in Matlab. To balance image information entropies, feature match quantities and signal-noise-ratio (SNR), the ClipLimit is recommended in 0.01–0.1. Specific values were not strictly limited but we found in these steps, original image pair information difference on illuminations and sensors could be eliminated. Ambiguity was set for pyramid matching and increased with flowing channel width which reached maximum on Thwaites Glacier and Larsen Ice Shelf. All factors which influence the images and the matching procedures are listed in Table 1. Hierarchical matching strategy significantly detailed velocity spatial patterns, ensured correction and analysis on them as in results and discussions, and ensured that our method could be independent from reference ice velocity map, providing unique ice velocity records on Larsen Ice Shelf, Thwaites Ice Tongue and Land Ice Tongue which had suffered a large portion of calving in following years.

Table 1 Factors and options for settings which affect matching results

Factors	Options
Orthorectified image components	1, 2 (max for MSS cross orthorectification), 3, 4 (max for TM belt orthorectification)
Match chip size (pixel)	8, 16, 32
Search distance threshold	Max displacement, half, quarter, eighth
Grid interval	Full of chip size, half, quarter
Contrast (ClipLimit)	0.01, 0.02, 0.05, 0.10
Ambiguity (oversize chip)	1×, 2×, 4×, 8×, 16×, 32×
Match type	Manual, feature, grid

2.5.2 Mismatch elimination and processing strategy

For historical image pairs, the presence of noise and a global lengthy search distance could result in a large portion of incorrect displacement tracking matches. To address this challenge, mismatch elimination steps were implemented, incorporating both internal self-calibration methods and external calibration methods for efficiency and extra temporal consistency. The execution sequence of mismatch elimination methods and the types of eliminated mismatches are shown in Figure 3.

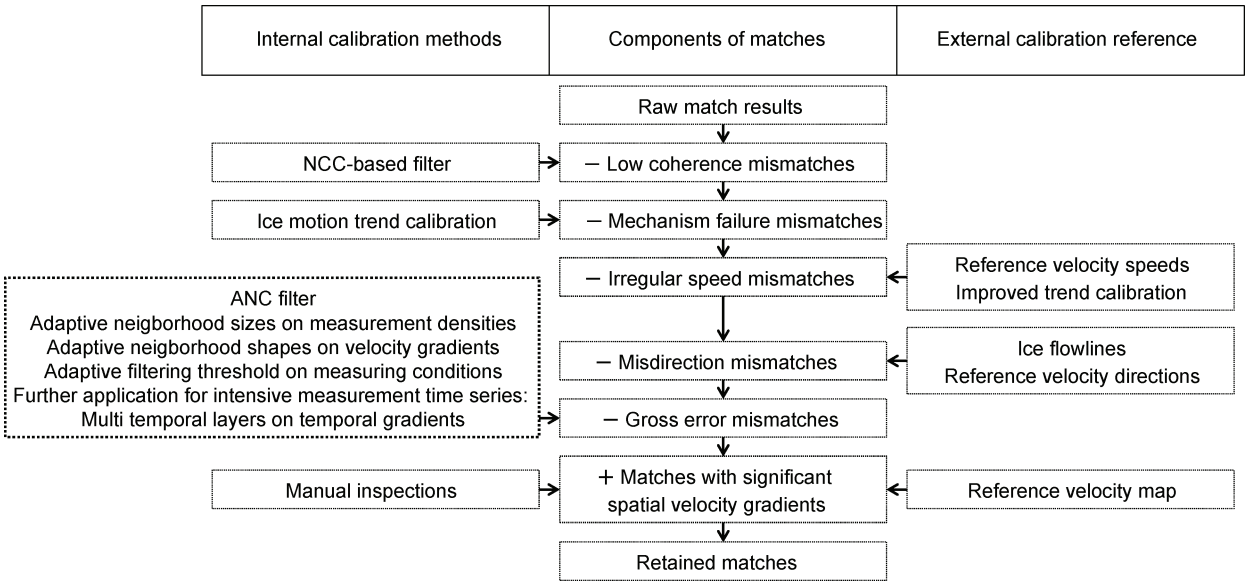

Figure 3 Processing strategy of mismatch elimination methods and types of eliminated mismatches in our research.

As the initial method, an NCC-based filter was designed to eliminate low-coherence noise mismatches (Feng et al., 2023). The second method, referred to as ice motion trend calibration, utilized terrain information from the DEM and the initial velocity field constructed by manual matches. These inputs provided prior constrains, allowing the identification of fast-flowing and stable regions to detect abnormal ice motions. Mismatches reflecting mechanism failures were identified and eliminated. Residual matches located in illogical positions, such as within heavy clouds and seawater regions, were removed from consideration. The principles guiding advanced calibration methods revolve around correcting speeds, directions, or velocity components of the velocity measurements. Detailed irregular mismatches on speeds and flowing directions were conducted by leveraging the temporal coherence of measurements, which was systematically provided through different issues of matches and reference velocity maps in subsequent years. A set of angle difference tolerance thresholds could be confirmed to remove outlier mismatches of misdirection types. The thresholds were adjusted to be much more varied, especially

on PIG where greater ice shelf instability and faster maximum flow speeds were observed.

The final systematic method employed is the adaptive neighboring correlation (ANC) match filter. Neighborhood radius is adaptive on match density which is first at 2 km for simulation of a 5×5 neighborhood matrix. The radius of neighborhood could be increased up to 6 km to collect enough retained velocity vector matches. Values of velocity properties (velocity values and velocity directions) in the neighborhoods were statistics for correlation analysis. Confidence interval was set as triple the standard deviation off mean and middle values. Velocities stayed within confidence intervals could pass the filter. In other words, velocities were accepted if they fell within about 90% when checked against the mean absolute deviation, regarding as Gaussian distribution (Liu et al., 2012). In regions with the fastest ice flow, such as PIG and Thwaites Glacier in West Antarctica, an optimized ANC match filter was implemented. This enhanced filter specifically compared the components of velocities in the *X*-axis and *Y*-axis directions in the polar stereographic perspective. The gradients of V_x and V_y in the *X* and *Y* axes could vary significantly. To filter velocity components, the neighborhood should collect approximate value differences in all directions. We considered the first order gradients of V_x and V_y to shape the neighborhood size, the minimum length of the short axis was set to 1 km, while the maximum length of the long axis was set to 6 km. The ratio of long and short axes was adjusted to be close to the gradients in the *X* and *Y* axes, which is usually vary for V_x and V_y. The improved ANC filter adaptively reduced the standard deviation caused by neighbor inconsistency and achieved higher accuracy. ANC filter should perform better when temporal correlation of velocities was added. In strategy of mid-year nominal timing for annual ice velocity maps, ANC would collect measurements up-downstream with adaptive distance on multi-temporal layers and by ice velocity temporal gradients.

The concluding method involved manual inspections, where matches exhibited obvious velocity spatial trends in the neighborhood, which might not pass ANC filter, could be retained. Manual inspection facilitated a comparative analysis between homonymous manual and automated matches, helping to identify and address uncertainties in the matches.

2.6 Map generation and adjustments

We generate velocity map by natural neighbor (NN) interpolation in 1 km resolution. The interpolation domain was carefully edited to fit distribution of measurements, considering the continental coastal boundary and ice boundaries. Initial velocities were computed as both temporal and spatial averages. We put measurements at start positions and considered timespans of map components that ranged from nearly 1 a to over 10 a. The above limitations resulted in velocity overestimations (OEs), particularly in areas with significant spatial acceleration. Li et al. (2022) provided clear evidence of OEs through space geometry and mathematical analysis. To address these OEs, adjustments were made by conducting a thorough spatial characteristics distribution analysis of the initial ice velocity map following two premises. An annual track algorithm was adapted to compute the OEs which is limited to fit regions where the maximum velocity did not obviously exceed 1 km·a^{-1}. In regions such as Thwaites Glacier and PIG, where the maximum velocity exceeded 2.5 km·a^{-1} and the timespan was only about 1 a, the algorithm was optimized to track at intervals of 0.2 a. The adjustment made to the OEs primarily focused on restoring correct velocity gradients especially in regions near the grounding line.

2.7 Criteria of accuracy estimations

2.7.1 Accuracy levels

Ideal target for quantizable residual error threshold of raster is a pixel. Acknowledging certain unverifiable error estimation limitations, the highest level (Level 2) for the limit of uncertainty is referred as “in (nearly) a pixel”. When error might be overestimated, transferred and assembled in steps, the synthetic uncertainties were at the lower acceptable level (Level 1) as “in limited pixels”. In terms of accuracy, the velocity interpolation and adjustment aim for Level 2 in individual steps, with the final accuracy of ice velocity map predominantly reaching Level 1, and in optimal portions, achieving Level 2 (Table 2).

Table 2 A summary of the uncertainties in the velocity field and their quantity levels

Levels of quantity	Uncertainty types	Geolocation	Imperfect match	Measuring conditions
Level 2	In (nearly) a pixel	ARGON mosaic	With remarkable features	Dense correct matching
Level 1	In limited pixels	Most TM images	With constraint	Matching vacancies in small area
Level 0	Not quantitative	Most MSS images	Without constraint	Matching vacancies in large area

2.7.2 Accuracy of ice velocity measurements

In this study, we evaluate the accuracy of velocity measurements by calculating their uncertainty components. The geolocation uncertainties of matching orthoimages are defined as σ_{ref} for base reference image and σ_{src} for searching target image. For image feature description, the identification uncertainties are defined as σ_{idn} estimated at one pixel. Regarding matching accuracy, the uncertainty is defined as σ_{mtc} and is estimated by manual inspections or inferred through mismatch elimination strategies and filtering parameter sets. The timespan is expressed as Δt. In

most scenes, the involved uncertainties are independent of each other. The ice flow velocity measuring uncertainty can be estimated as follows:

$$\sigma_{\mathrm{vlc}} = \frac{1}{\Delta t}\sqrt{\sigma_{\mathrm{ref}}^2 + \sigma_{\mathrm{src}}^2 + \sigma_{\mathrm{idn}}^2 + \sigma_{\mathrm{mtc}}^2} \quad (1)$$

For ice velocity measurements in this study, the theoretical values of σ_{vlc} range from 4 m·a^{-1} to 120 m·a^{-1}.

2.7.3 Accuracy estimations on matching

To discuss the accuracy of matching, a correct match is defined as one where the matched points reached the NCC peak within a very limited region containing the historical displacement truth on orthorectified image pairs. However, a large portion of matches may deviate from the actual displacements as imperfect matches. There are two main types of imperfect matches.

Type I: Offset match. The matched points are located in the same glaciology feature structures, but the displacements are not accurate enough due to inhomogeneous structure deformation (rotation, small-scale calving, etc.), shade effects or resolution-limited feature descriptions.

Type II: Miss target. The matched points were located in different (usually adjacent) glaciology feature structures due to different temporal cycles and continuous distributed similar glaciology feature patterns. However, in such cases, the errors of miss-target correct matches are smaller than those of offset matches, mainly due to discrepant solar azimuth or rotation and transformation of the structures.

To assess matching accuracy qualitatively, we considered that the maximum error could reach half the size of recognizable glaciology feature structures. For the distribution of matching accuracy, the offset matches along crevasses and rifts in the smoothed-edged regions were almost evenly distributed. The miss target matches perpendicular to linear structures followed an approximately Gaussian distribution. The offset matches perpendicular to linear structures were unable to be optimized without accurate DEM in the corresponding time. The miss target matches along linear structures depended on the sub-structure feature conditions which were mainly affected by image resolution. Moreover, in image series, errors of offset matches perpendicular to linear structures did not transmit over pairs, whereas errors along linear structures and miss target matches could accumulate over matching image pairs and maps synthesis.

2.7.4 Accuracy estimations on mapping and adjustments

The accuracy of mapping was affected by both the accuracy of ice velocity measurements and the difference between velocity variation ground truth and velocity interpolation. NN reduced the factors on interpolation to three measurements and linear plane fitting. When the pixel size is relatively large, the hybrid velocity would be closer to the actual velocity but with smoother velocity gradients. Therefore, improving fitting accuracy and adjustment accuracy simultaneously may pose a challenge. The residual errors on OE adjustment were almost at the same level as matching errors. As a result, we usually corrected OE only when they exceeded 1.5 times the theoretical error (1.5 σ).

3 Results and discussions

3.1 Research outputs and accuracy levels

In this study, our first outputs are series of orthorectified historical Landsat images in Level 2. Our primary product is the trans-glacier cross-decade synthetic ice velocity map in West Antarctica, of which the velocity measurements were densified and corrected to address overestimations. Utilizing the ANC filter, we set the maximum neighboring radius to 6 km. Where there were measurements right inside map pixels, the mapping accuracy is categorized as Level 2. When measurements are within 6 km with a negligible matching vacancy and a proper velocity variation tendency, the mapping accuracy is classified as Level 1. Our synthesized map in West Antarctica, with restricted uncertainty, is displayed in Figure 4. Besides a few ice velocity map components from TM image pairs in a year-round and pairs with MSS image in two years, most one-sigma velocity theoretical errors were under 60 m·a^{-1}.

3.2 Analysis of velocities along profiles and OE distributions

Here we listed four accelerated fastest glaciers (Land Glacier, Hull Glacier, Thwaites Glacier, PIG) to show our results on ice velocity measurements and overestimations (Figure 5) with comparison to synthesis InSAR-based Antarctic ice velocity map measured in 1996–2016 from multi-sensors (Rignot et al., 2017).

3.2.1 Overall situation about velocities and comparisons along profiles and OEs

Profiles A-A', B-B', F-F' extend longitudinal along the mid-positions of the ice flow direction on Land Glacier, Hull Glacier and PIG. Profiles C-C', D-D' run longitudinally towards the maximum velocity during different periods on Thwaites Glacier. Profile E-E' is about latitudinal. Points were sampled every 500 m, and velocities from this study were smoothed at 1 km interval to achieve sub-pixel resolution on the map. During the periods in which most velocities were measured, along with the maximum theoretical measurement errors according to Equation (1), the shortest timespan and image resolutions are summarized in Table 3. Observations for InSAR measurements were in repeat cycle of 1 to 46 d, adopted speckle tracking and phase interference technologies required short time-lapses, which made InSAR-based ice velocities (most from sub-map-resolution/under 450 m displacements) almost instantaneous compared with our results. Along these profiles, spatial accelerations and decelerations caused by terrain slope were observed upstream, aligning with the strategy of

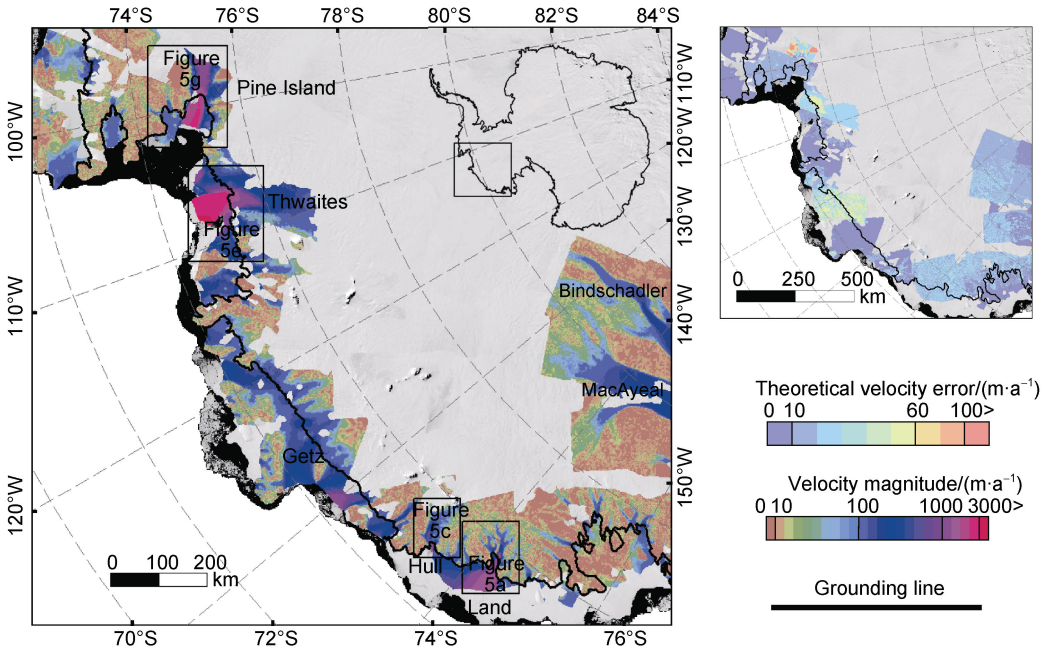

Figure 4 Reconstructed historical ice velocity field along the coast with the most ice-discharged outlets in West Antarctica (the locations of representative glaciers introduced in Section 3.2 and detailed in Figure 5 are framed). The grounding line shown here and in later sections was adopted and updated from Gardner et al. (2018).

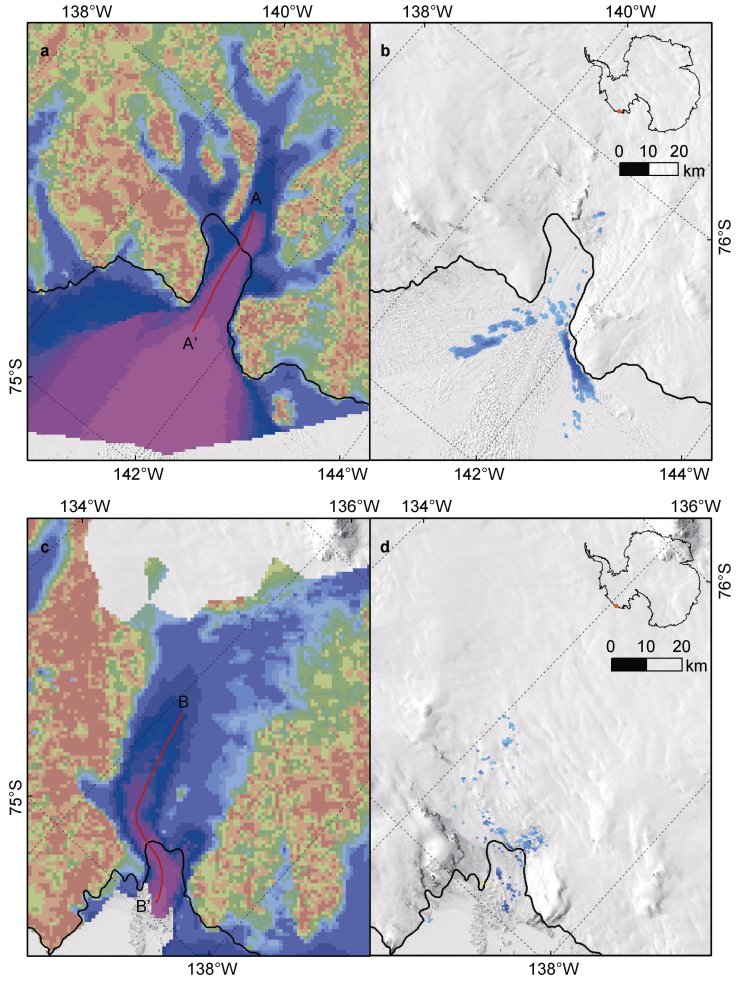

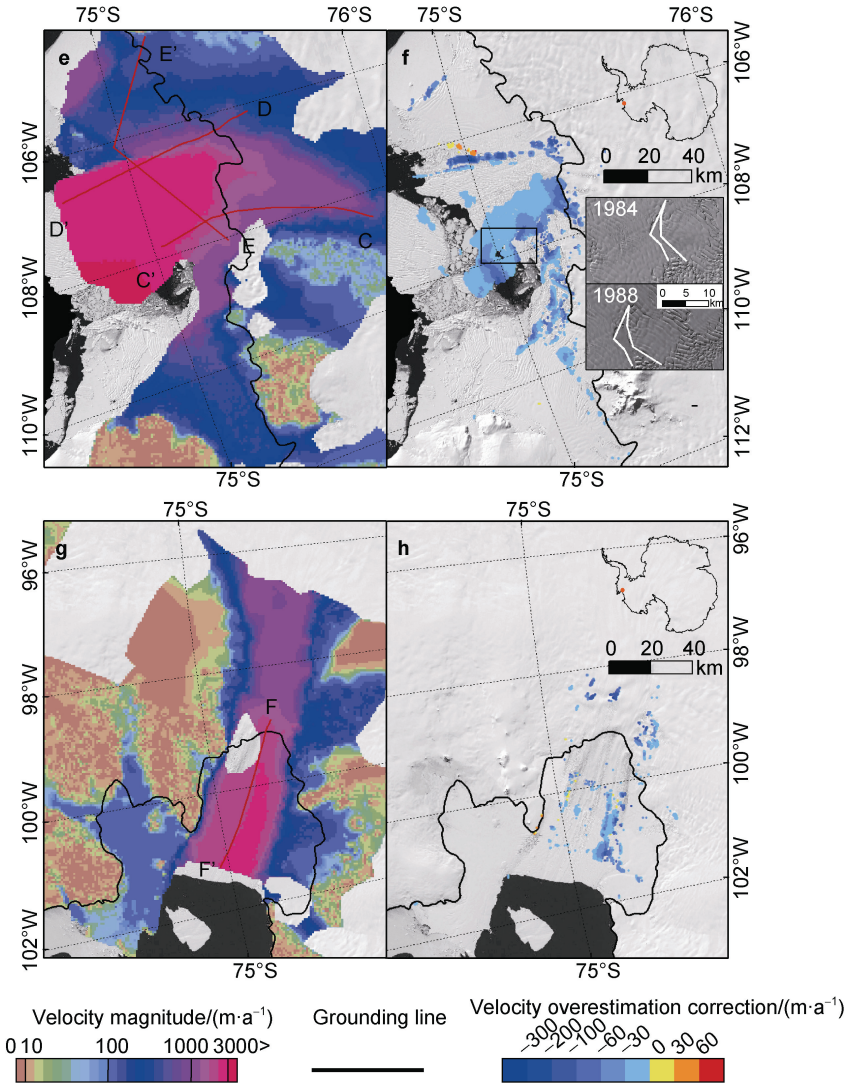

Figure 5 Ice velocities, profiles and overestimation corrections displayed over LIMA on Land Glacier (**a**, **b**); Hull Glacier (**c**, **d**); Thwaites Glacier (**e**, **f**); PIG (**g**, **h**). Overestimations were not fully corrected on Thwaites Glacier enclosed region due to developmental rifting between 1984 and 1988 (sub-figure in **f**), further separated local ice shelf boundary lines were shown in white.

Table 3 Statistical results of ice velocity comparisons and overestimation corrections on typical glaciers

Glacier	Profile	Periods with the densest measurements	Maximum theoretical error/(m·a^{-1})	Average velocity difference/(m·a^{-1})	Average overestimation correction/(m·a^{-1})
Land	A-A’	1986–1988	32	+88	−47
Hull	B-B’	1984–1988	32	+115	−43
Thwaites	C-C’	1984–1988	55	+58	−45
	D-D’			+907	
	E-E’			+441	
Pine Island	F-F’	1986–1989	66	+1489	−45

locating measurements on reference images (Figure 6). Hence, spatial delayed accelerations on ice shelves might indicate the shrinkage of stable areas. In the first half of profile C-C’ and the second half of profile B-B’, velocities in this study were not fully manually inspected. Obvious glaciology features were not along flow well distributed on Hull Glacier and not distinguishable on upstream part of Thwaites Glacier. The abnormal acceleration and deceleration on the tail of B-B’ were caused by the calving ice front not fully detaching, which began between 1987 and 1988. Along C-C’, there were obvious temporal accelerations upstream. When ice went on Thwaites Ice Tongue, step-like spatial ice velocity accelerations along C-C’ on the ice shelf mainly occurred with developing rifting.

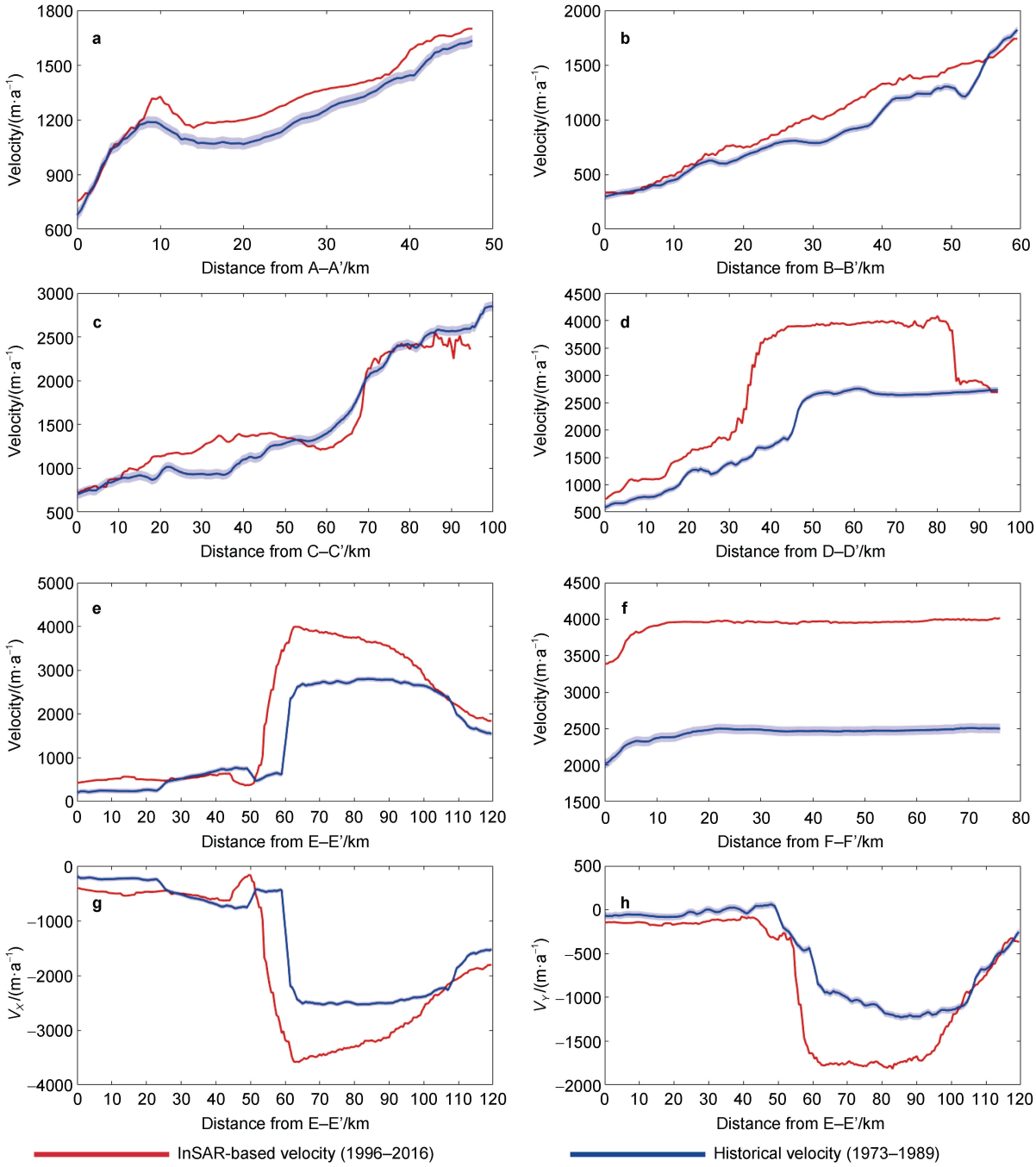

Figure 6 Ice velocity comparisons along profiles A-A' to F-F' on (**a**–**f**), V_x (**g**) and V_y (**h**) along E-E' were additionally compared for further discussion.

Here, we regard the regions where ice velocity (components) reached the highest level as the most unstable, while the rest are relatively stable areas. Velocities along D-D' and E-E' clearly indicated significant shrinkage of stable area on Thwaites. Velocity spatial distribution and patterns were transferred, and velocity directions were partially skewed due to structure deformation. Without considering spatial smoothing, profile D-D' showed a longitudinal shrinkage of about 15 km, and profile E-E' showed a latitudinal shrinkage of about 10 km on Thwaites Ice Tongue. Velocity temporal analysis on PIG had been further discussed (Liu, et al., 2022), and the ice shelf structure appears to be much more stable than Thwaites Glacier in this period, although temporal accelerations in these two glaciers were most significant.

3.2.2 Discussions about velocity gradients and OEs

Compared with velocity measurements derived from short time-lapse image pairs, the temporal averaged velocity measurements in this study might lose detailed flow

patterns in terms of directions and gradients and may contain uncorrected errors due to image resolution limitations. Similarly, measurements from all short time-lapse image pairs filmed during austral summer days might include seasonal overestimations compared to the annual average ice velocity field. For the introduced spatial overestimations, two main phenomena can mislead their corrections. Corrections depend on the premise that ice velocity field was continuously consistent. One phenomenon is the development of rifts, and the other is the intersections of two ice flows with different initial directions. Ice flows meeting upstream grounding line would fuse together, while those intersecting on ice shelves would take different paths. Curved ice flows around huge islands meet and converge into a unified middle flow direction on Ross and Getz ice shelves. Ice flows intersected on ice shelf downstream of Land Glacier move in different velocity layers. Incomplete calving and rifting could be regarded as a falling behind of ice blocks upstream, which is contradictory to the overestimation correction premise.

Overestimations in these areas could not be accurately addressed with warped velocity gradients, for example the rifting on Thwaites Ice Tongue that developed in 1984–1988 (Figure 5e). In this study, the average corrected OEs in representative glaciers were all about 45 $m \cdot a^{-1}$ (Table 3), highly affected by similar timespans of image pairs on these glaciers. The average value could not illustrate spatial acceleration patterns. Conversely, overestimations revealed the instability of ice shelves, as the horizontal strain rate tensor is highly dependent on velocity gradients. Where ice velocities varied more spatially, ice suffered more driving strain. We compared our OE corrections with ice front lines on Thwaites Glacier (Figure 7). Local lines in 2001–2003 were mapped manually from MODIS imagery in March of each year (Miles et al., 2021). MODIS satellite data were used to measure the change in ice shelf calving front position as complete lines in 2012–2013 (Andreasen et al., 2023), and local lines mapped from LIMA were produced in this study.

Images in 1973 and 1984 captured the calving of the entire ice tongue of Thwaites. Ice front lines recorded such events between 2001/2002 and 2012/2013 on an annual scale, indicating that the calving cycle of Thwaites is about 11 a. Even though these calving events led to unrecoverable ice shelf area reduction over decades. Further smaller-scale ice front line transformations were automatically monitored monthly from Sentinel-1 data starting in 2014 by the German Aerospace Center (2022). For OEs in 1984–1988, the distribution of the highest OEs along the extension of profile C-C' showed where ice shelf structure weakened, pointing out where the strain rate would accumulate, and the entire calving for Thwaites Ice Tongue in 2001/2002 and local calving in 2002/2003 occurred in these places, reshaping the ice front along the extreme value distributions of OEs.

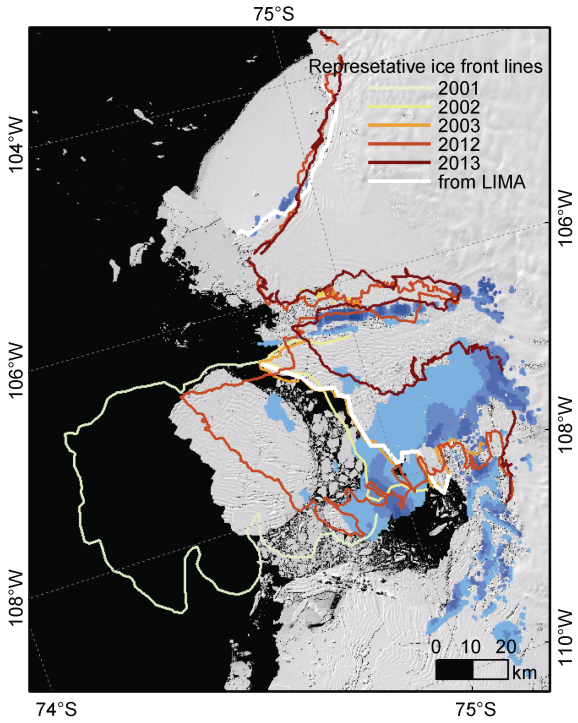

Figure 7 Ice velocity overestimation corrections on Thwaites Glacier in the 1980s with multi-source calving-relevant ice front lines displayed over LIMA color coded in different years.

The entire distribution of OEs on Thwaites reflects the instabilities of the entire ice tongue, ultimately leading to calving in 2012/2013. We believe this could serve as evidence for forecasting calving events about 30 a in advance. For the eastern Thwaites Ice Shelf, the OE distribution could only track the calving ice front for about 15 a of LIMA. In the shear zone between Thwaites Ice Tongue and eastern Thwaites Ice Shelf, the OE distribution indicates instability in the inner-front ice structure, while the damaging and calving would be less traced given the main flow direction of Thwaites Ice Tongue, where there was more feeding and buttressing ice discharge. For other representative glaciers, longitudinal-distributed OEs on PIG showed major strain rate in edge regions of high-speed flow. OEs on Land Glacier and Hull Glacier also gather where ice flow turned around and meeted with flow from other outlets, and where ice shelf and ice tongue structures weakened. Considering with measuring conditions, the image resolutions in this study, major glaciology feature marks were latitudinal on eastern Thwaites Ice Shelf, longitudinal along main flow lines on PIG, Land Glacier and Hull Glacier, mixed and gathered on Thwaites Ice Tongue, where ice tributaries fed the main ice flow on PIG, Land Glacier, and Hull Glacier, and where near the ice front and outlets were widely open on Land Glacier and Hull Glacier.

4 Conclusion

Using an adaptive combination of techniques and

methods, we have successfully reconstructed the historical ice velocity field from optical satellite images, achieving a one-sigma accuracy less than 60 $m \cdot a^{-1}$ in most coastal regions of West Antarctica. Given the much denser ice velocity measurements, the ongoing debate on the estimation of ice mass balance before 1990 would benefit from the results of this study, as it helps to refine estimates of ice discharge. We emphasize that both temporal changes in ice velocities and their spatial distribution could provide insights into the instabilities of ice shelves. In addition to potential ice discharge overestimations due to ice velocity OEs in the grounding zone, the OEs reflected the historical along-flow strains in specific ice shelf formations. Velocity OEs on Thwaites Ice Tongue in the late 1980s had revealed the positions of the calving front for the next 3 times as the Haynes ice front retreated and the Crosson and Thwaites shelves separated. Estimates of calving risk and temporal responses are crucial for accurate modeling and prediction of ice dynamics across the entire Antarctica.

Acknowledgements This work was supported by the National Key Research and Development Program of China (Grant no. 2021YFB3900105). We thank the support from the Fundamental Research Funds for the Central Universities and the support by the National Key Research and Development Program of China (Grant no. 2017YFA0603100). We thank Kee-Tae Kim for the provision of the ARGON mosaic and coastline products of Antarctica (https://etd.ohiolink.edu/apexprod/rws_etd/send_file/send?accession=osu1072898409&disposition=inline), and also acknowledge the United States Geological Survey (USGS) for Landsat images (https://earthexplore.usgs.gov/) and LIMA (https://lima.usgs. gov/), and the National Snow and Ice Data Center for RAMP DEM version 2 (https://doi.org/10.5067/8JKNEW6BFRVD). We appreciate Dr. Gang Li as reviewer and one anonymous reviewer, Associate Editor Dr. Jon Ove Hagen for the constructive comments that helped to improve the manuscript.

References

Andreasen J R, Hogg A E, Selley H L. 2023. Change in Antarctic ice shelf area from 2009 to 2019, Version v1. (2023-04-14)[2023-11-14]. doi:10.5281/zenodo.7830051.

Bindschadler R A, Vornberger P, Fleming A, et al. 2008. The Landsat image mosaic of Antarctica. Remote Sens Environ, 112(12): 4214-4226, doi:10.1016/j.rse.2008.07.006.

Feng T T, Li Y J, Wang K L, et al. 2023. A hierarchical network densification approach for reconstruction of historical ice velocity fields in East Antarctica. J Glaciol, 69(274): 281-300, doi:10.1017/jog.2022.58.

Gardner A S, Moholdt G, Scambos T, et al. 2018. Increased West Antarctic and unchanged East Antarctic ice discharge over the last 7 years. Cryosphere, 12(2): 521-547, doi:10.5194/tc-12-521-2018.

German Aerospace Center (DLR). 2022. IceLines–Ice shelf and glacier front time series. Munich: German Aerospace Center, doi:10.15489/btc4qu75gr92.

Gerrish L. 2020. Automatically extracted rock outcrop dataset for Antarctica (7.3). UK Polar Data Centre, Natural Environment Research Council, UK Research & Innovation, doi:10.5285/178ec50d-1ffb-42a4-a4a3-1145419da2bb.

Heid T, Kääb A. 2012. Evaluation of existing image matching methods for deriving glacier surface displacements globally from optical satellite imagery. Remote Sens Environ, 118: 339-355, doi:10.1016/j.rse.2011.11.024.

Howat I M, Porter C, Smith B E, et al. 2019. The reference elevation model of Antarctica. Cryosphere, 13(2): 665-674, doi:10.5194/tc-13-665-2019.

Hui F M, Ci T Y, Cheng X, et al. 2014. Mapping blue-ice areas in Antarctica using ETM+ and MODIS data. Ann Glaciol, 55(66): 129-137, doi:10.3189/2014aog66a069.

Kim K T. 2004. Satellite mapping and automated feature extraction: Geographic Information System-based change detection of the Antarctic coast. Thesis (Ph.D.), Columbus: The Ohio State University.

Li R X, Ye W K, Qiao G, et al. 2017. A new analytical method for estimating Antarctic ice flow in the 1960s from historical optical satellite imagery. IEEE Trans Geosci Remote Sens, 55(5): 2771-2785, doi:10.1109/TGRS.2017.2654484.

Li R X, Cheng Y, Cui H T, et al. 2022. Overestimation and adjustment of Antarctic ice flow velocity fields reconstructed from historical satellite imagery. Cryosphere, 16(2): 737-760, doi:10.5194/tc-16-737-2022.

Li R X, Cheng Y, Chang T, et al. 2023. Satellite record reveals 1960s acceleration of Totten Ice Shelf in East Antarctica. Nat Commun, 14(1): 4061, doi:10.1038/s41467-023-39588-x.

Liu H, Jezek K C, Li B, et al. 2015. Radarsat Antarctic Mapping Project Digital Elevation Model, Version 2. (2015-12-03)[2023-12-12]. Boulder: NASA National Snow and Ice Data Center Distributed Active Archive Center, doi:10.5067/8JKNEW6BFRVD.

Liu H X, Wang L, Tang S J, et al. 2012. Robust multi-scale image matching for deriving ice surface velocity field from sequential satellite images. Int J Remote Sens, 33(6): 1799-1822.

Liu S J, Su S, Cheng Y, et al. 2022. Long-term monitoring and change analysis of pine island ice shelf based on multi-source satellite observations during 1973–2020. J Mar Sci Eng, 10(7): 976, doi:10.3390/jmse10070976.

Miles B, Stokes C, Jenkins A, et al. 2021. Thwaites ice front position shapefiles 2000–2018 (Version 1.0). [2023-11-11]. UK Polar Data Centre, Natural Environment Research Council, UK Research & Innovation, doi:10.5285/1355A656-2B8D-4E95-B524-BFC1A7C686FB.

Rignot E, Mouginot J and Scheuchl B. 2017. MEaSUREs InSAR-based Antarctica ice velocity map, Version 2. (2017-04-20) [2023-10-11]. Boulder: NASA National Snow and Ice Data Center Distributed Active Archive Center, doi:10.5067/D7GK8F5J8M8R.

Toutin T. 2004. Geometric processing of remote sensing images: models, algorithms and methods. Int J Remote Sens, 25(10): 1893-1924, doi:10.1080/0143116031000101611.

Wang S J, Liu H X, Yu B L, et al. 2016. Revealing the early ice flow patterns with historical declassified intelligence satellite photographs back to 1960s. Geophys Res Lett, 43(11): 5758-5767, doi:10.1002/2016gl068990.

Wang S J, Liu H X, Jezek K, et al. 2022. Controls on Larsen C Ice Shelf retreat from a 60-year satellite data record. J Geophys Res: Earth Surface, 127(3): e2021JF006346, doi:10.1029/2021jf006346.

Yuan X H, Qiao G, Li Y J. 2023. 57-year ice velocity dynamics in Byrd Glacier based on multisource remote sensing data. IEEE J Sel Top Appl Earth Obs Remote Sens, 16: 2711-2727, doi:10.1109/JSTARS.2023.3250759.